Power-Law Scaling of Early-Stage Forces during Granular Impact

Nasser Krizou and Abram H. Clark
Department of Physics, Naval Postgraduate School, Monterey, California 93943, USA

(Received 18 December 2019; accepted 13 April 2020; published 29 April 2020)

We experimentally and computationally study the early-stage forces during intruder impacts with granular beds in the regime where the impact velocity approaches the granular force propagation speed. Experiments use 2D assemblies of photoelastic disks of varying stiffness, and complimentary discrete-element simulations are performed in 2D and 3D. The peak force during the initial stages of impact and the time at which it occurs depend only on the impact speed, the intruder diameter, the stiffness of the grains, and the mass density of the grains according to power-law scaling forms that are not consistent with Poncelet models, granular shock theory, or added-mass models. The insensitivity of our results to many system details suggests that they may also apply to impacts into similar materials like foams and emulsions.

DOI: 10.1103/PhysRevLett.124.178002

High-speed impact by an intruder into a granular bed [1] has broad relevance in many disciplines, including ballistics [2–5], robotics [6,7], astrophysics [8], and earth science [9]. The forces exerted by the grains on the intruder are often well described by Poncelet models, which are dominated by a velocity-squared drag force [10–13]. However, the initial impact forces are consistently larger than expected from these models [4,13–19]. Very little is known about these early-stage forces, particularly in the high-speed regime where the impact speed v_0 approaches a characteristic force propagation speed in the granular bed v_b. In this Letter, we use experiments and simulations to study the early-stage forces in this regime. We find that the peak forces and associated times obey simple, power-law scaling forms that depend only on the impact speed, the intruder diameter, the stiffness of the grains, and the mass density of the grains. These scaling laws do not fit within the framework of any existing theory related to impact, including Poncelet models, granular shock theory, and added-mass models.

Experiments involve circular intruders falling due to gravity and striking a collection of more than 10 000 photoelastic disks. These experiments have been used previously to study the microscopic origins of Poncelet drag [16,17,20], as well as the speed and spatial structure of the propagating forces [21]. Intruders are bronze disks with diameters $D = 6.35$, 12.7, and 20.32 cm and masses of $M = 0.062$, 0.258, and 0.671 kg, respectively. We also cut one circular intruder out of aluminum with diameter $D =$ 12.7 cm with $M = 0.076$ kg. Photoelastic particles are made from three different materials of varying stiffness, as described in Ref. [21]. For all particles, the force f required to compress a particle by a distance δ is experimentally found to obey $f = E^* w d(\delta/d)^\alpha$, where $\alpha \approx 1.4$, $w = 3$ mm is the particle thickness, d is the particle diameter, and E^* is an effective Young's modulus. We find $E^* \approx 3$, 23, and 360 MPa for soft, medium, and hard particles, respectively. We use bidisperse mixtures: hard particles have $d = 4.3$ and 6 mm, and medium and soft particles have $d = 6$ and 9 mm. We find bulk densities $\rho_g \approx 1100$ kg/m^3 for all three types of particles. The velocity scale for propagating forces is set by $v_b = \sqrt{E^*/\rho_g} \approx 52$, 145, and 572 m/s for soft, medium, and hard particles, respectively [21]. Initial impact speeds are $0.3 < v_0 < 6$ m/s, meaning that we experimentally access impact speeds in the range $10^{-3} < v_0/v_b < 10^{-1}$. We record results with a Photron FASTCAM SA5 at frame rates of 10 000, 25 000, and 40 000 frames per second for soft, medium, and hard particles, respectively. Intruder trajectories are determined by tracking the position z of the intruder ($z = 0$ represents the impact point, and downward is positive z) at each image; sample images and trajectories are shown in Fig. 1. Since discrete differentiation of noisy data requires a low-pass filter, we cut off some high-frequency data in the intruder velocity $v = dz/dt$ and acceleration $a = d^2z/dt^2$, and we use a calibrated photoelastic signal as a secondary source of force information.

Figure 1 shows photoelastic images along with corresponding trajectory plots during impacts into medium particles (a video can be found in the Supplemental Material of Ref. [21]). We observe similar phenomenology for soft particles, as shown in the Supplemental Material [22]. The force exerted by the granular material onto the intruder shows a clear buildup to a maximum $F_{\max}$ on the intruder at time $t_{\max}$ (frame 3). After this, the shock wave continues to propagate down into the material, but the force on the intruder begins to relax. The force from tracking the intruder (thick black curve) and from the photoelastic signal (thin blue curve) show good agreement, confirming that we are not missing any high-frequency dynamics from the low-pass filtering of the trajectory. System boundaries

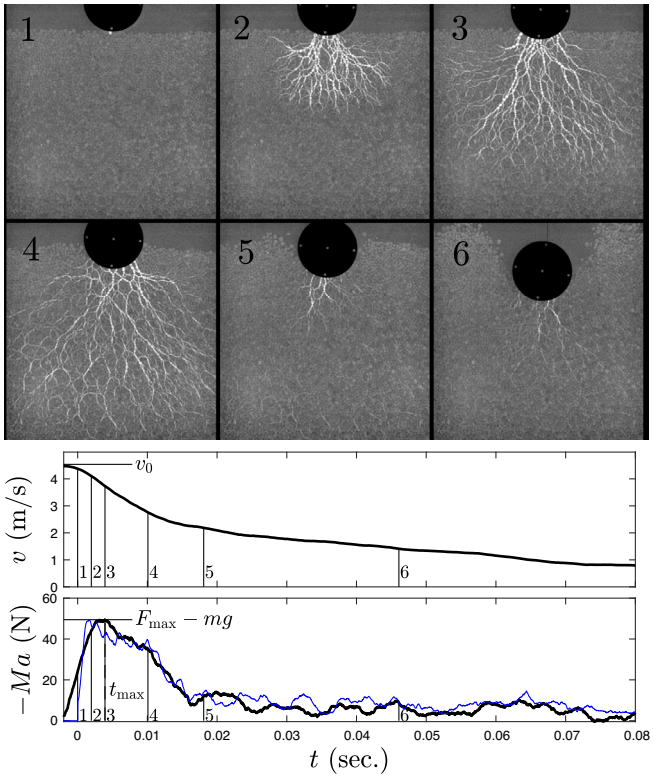

FIG. 1. Photoelastic image sequences are shown for an impact of the bronze intruder with $D = 12.7$ cm at $v_0 \approx 4.4$ m/s into medium particles (soft particles are shown in the Supplemental Material [22]), with corresponding trajectories shown below. Times marked 1–6 correspond to images 1–6 shown above. The thick black curve comes from tracking the intruder, and the thin blue curve is a time series of the total calibrated photoelastic response in a region beneath the intruder.

do not affect our results: the boundary of the experiment is roughly 5 particle diameters below the bottom of the image, and the sidewalls are more than 20 particle diameters outside the edges of the image shown, so the shock front at $t_{\max}$ has not reached the boundaries in any direction. We also verify that boundaries do not affect our results using simulations by varying system size over a large range.

Figure 2(a) shows typical experimental trajectories. We plot v and $-Ma$ with respect to time after impact, and then record $F_{\max} = -Ma_{\max} + Mg$, where $g = 9.81$ m/s^2, and $t_{\max}$ as a function of v_0, as plotted in Figs. 2(b) and 2(c). These reveal power-law scaling for $F_{\max}$ and $t_{\max}$ versus v_0: $F_{\max} \propto v_0^{4/3}$ and $t_{\max} \propto v_0^{-2/3}$. At small v_0, $F_{\max}$ appears to plateau as expected since $F_{\max} \approx Mg$ for very slow impacts, where the granular force will increase until it approximately balances the gravitational force. These measurements for soft and medium particles are unambiguous (photoelastic and tracking data agree well). Fast force dynamics for the hard particles, with $v_0/v_b < 10^{-2}$, cause $F_{\max}$ to be underestimated from only tracking the intruder [20], as seen in Fig. 2(a). The force from tracking the intruder [the thicker black line in Fig. 2(a)] has a clear peak slightly above 10 N during $0 < t < 0.01$ s, while the photoelastic signal [the thinner black line in Fig. 2(a)] shows a burst of peak forces: one above 50 N and four more around 30 N during this time. This is typical of all force measurements during impacts into hard particles. Thus, the data for hard particles in Fig. 2(b) is measured from video tracking and then multiplied by a constant correction factor (roughly 4.5) to account for this difference. The largest peak in the photoelastic signal is not always the first one, so we measure $t_{\max}$ from the video tracking data [e.g., $t_{\max} \approx 0.005$ in Fig. 2(a)], which represents the mean time associated with the burst of large forces observed in the photoelastic signal. Similar results are found by measuring $F_{\max}$ and $t_{\max}$ directly from the calibrated photoelastic data, but with significantly more scatter. The peak forces measured in this way for hard particles is similar to the data for soft and medium particles, as shown in Figs. 2(b) and 2(c), albeit with slightly different phenomenology: a burst of peak forces rather than a clear buildup and relaxation (this is also evident from videos in the Supplemental Material in Ref. [21]). This suggests a possible change in behavior for $v_0/v_b \ll 10^{-2}$. Previous studies using even stiffer grains [6,11] have sometimes found $F_{\max} \propto v_0^2$ for similar impact speeds $v_0 \sim 1$ to 5 m/s into, e.g., glass beads where $E^* \sim 50$–100 GPa, $\rho_g \sim 2000$ kg/m^3, and thus $v_0/v_b < 10^{-3}$.

To better understand the origins of the power-law behavior in Figs. 2(b) and 2(c), we perform discrete-element simulations [23,24] using C++ in 2D and LAMMPS [25] (http://lammps.sandia.gov) in 3D; further details are given in the Supplemental Material [22]. We prepare a static, gravitationally loaded bed of 10 000 grains in 2D and 100 000 grains in 3D, which we verify are large enough that system boundaries (lateral or bottom) do not affect our results in any way. Previous work has sometimes found that the initial packing fraction plays a role in the impact response [12,26] due to dilation (for densely prepared systems) or compaction (for loosely prepared systems) during shear. This effect is suppressed for frictionless grains [27]. Our results are not sensitive to the initial packing fraction of the bed or, as shown below, even to the existence of friction at all. Thus, we conclude that shear-induced dilation and compaction do not affect the scaling laws we show. After preparing the bed, we then put a circular (2D) or spherical (3D) intruder just above the bed with downward velocity v_0, after which it is free to accelerate due to forces from grains or gravity. We observe trajectories that are similar to those shown in Figs. 1 and 2(a), as well as throughout the literature [14,18]. We again find $F_{\max} \propto v_0^{4/3}$ and $t_{\max} \propto v_0^{-2/3}$, as shown in Fig. 3. At slow speeds, the power-law scaling is cut off by $F_{\max} \approx Mg$ since gravity accelerates the intruder and generates forces

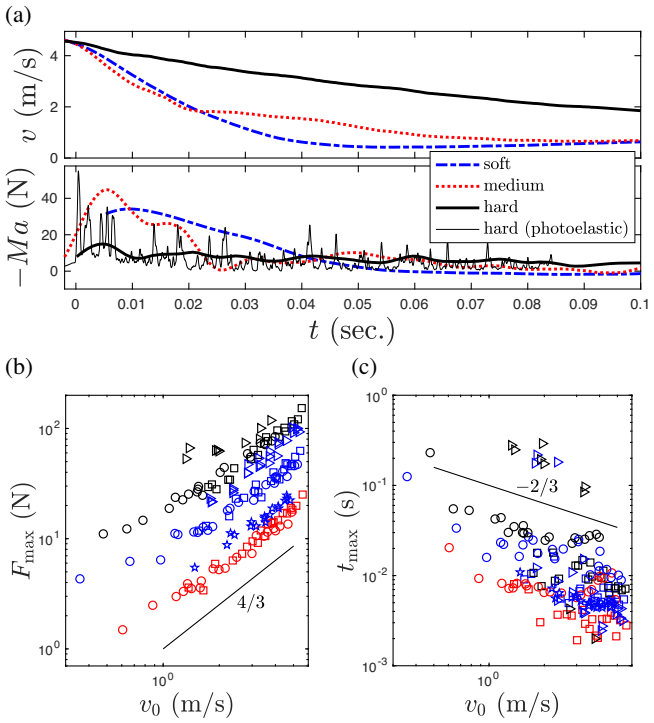

FIG. 2. (a) Sample trajectories for the bronze intruder with $D = 12.7$ cm impacting into hard, medium, and soft particles. The photoelastic force is obtained by calibrating a time series of the photoelastic response beneath the intruder [20]. (b) F_{max} and (c) t_{max} are then plotted as a function of v_0. Circles, squares, and triangles represent soft, medium, and hard particles (respectively) with bronze intruders. Stars represent impacts of aluminum intruders into soft particles. Red, blue, and black represent intruder diameters $D = 6.35$, 12.7, and 20.32 cm, respectively.

comparable to its weight. This occurs at longer t_{max}, nearly independent of v_0.

For 2D simulations of circular intruders impacting beds of frictional circular grains, there are nine system parameters: the intruder diameter D, mass M, and speed v_0; the grain diameter d, mass m, stiffness $K = E^* w$, friction coefficient μ, and force law exponent α; and the gravitational constant g. Masses per area for grains and intruder are $\sigma_i = \rho_i w = 4M/\pi D^2$ and $\sigma_g = \rho_g w = 4m/\pi d^2$, where ρ_i and ρ_g are the masses per volume and w is the thickness of the particles (w only has meaning in the experiments). Figures 3(a) and 3(b) show that the power-law scaling is nearly independent of both α and μ. The lack of dependence on μ suggests that dilation or compaction due to shear, which only occurs for frictional grains, does not affect our results (possibly because the material does not have time to develop any shear-induced dilation or compaction). Figures 3(c) and 3(d) show that the intruder weight Mg sets the value of the plateau, as expected, but does not affect the forces due to the power-law scaling, particularly once $\sigma_i/\sigma_g > 4$. We also find our results do not explicitly depend on d; this is implicitly shown in Fig. 4, which includes values of d that vary by an order of magnitude in 3D (however, we only study cases with $D \geq 5d$). The remaining quantities F_{max}, t_{max}, v_0, D, K, and σ_g form three dimensionless groups, F_{max}/KD, $t_{max} v_b/D$, and v_0/v_b, where $v_b = \sqrt{K/\sigma_g} = \sqrt{E^*/\rho_g}$. Figures 4(a) and 4(b) explicitly show that all our data for 2D frictionless Hookean simulations collapse when F_{max}/KD and $t_{max} v_b/D$ are plotted as a function of v_0/v_b. We note that the collapse in Figs. 4(a) and 4(b) includes data spanning 2 orders of magnitude in K, which was not explicitly shown in Fig. 3, but is shown in the Supplemental Material [22].

In 3D, grain-grain compression is governed by $f = E^* d^2 (\delta/d)^\alpha$ (along with frictional and dissipative intergrain interactions; see Supplemental Material [22]). We again find $F_{max} \propto v_0^{4/3}$ and $t_{max} \propto v_0^{-2/3}$, with a plateau at slow speeds set by $F \approx Mg$. The power-law behavior is again nearly independent of μ, α, g, d, and the mass per volume ρ_i of the spherical intruder (provided $\rho_i > \rho_g$). The remaining parameters F_{max}, t_{max}, v_0, E^*, D, and ρ_g form three dimensionless groups: $F_{max}/E^* D^2$, $t_{max} v_b/D$, and v_0/v_b,

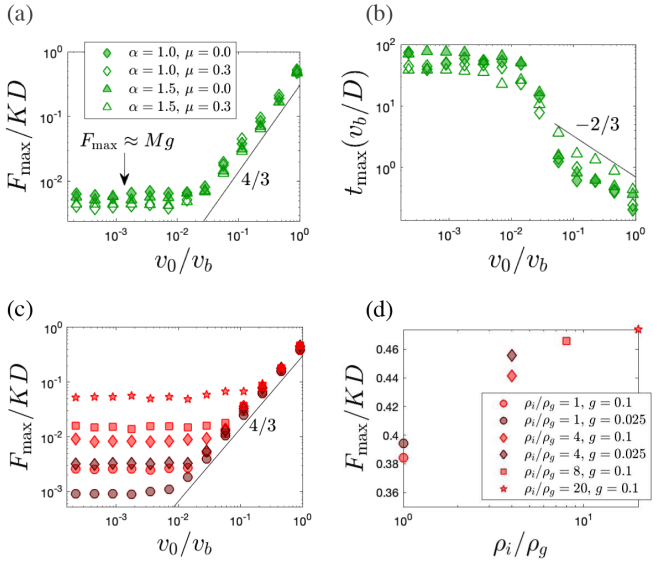

FIG. 3. (a) F_{max}/KD and (b) $t_{max}(v_b/D)$ are plotted as a function of v_0/v_b for 2D simulations with $D = 7$, $d = 1$, $\sigma_g = \rho_g w = 1$, $K = 785$, $\sigma_i = \rho_i w = 4$, and $g = 0.1$ with varying grain-grain friction coefficient μ and force law exponent α, showing that $F_{max} \propto v_0^{4/3}$ and $t_{max} \propto v_0^{-2/3}$ are independent of μ and α. The legend in (a) also applies to (b). (c) F_{max}/KD is plotted as a function of v_0/v_b for simulations with $D = 14$, $d = 1$, $\sigma_g = \rho_g w = 1$, $K = 785$, $\mu = 0$, $\alpha = 1$. The power-law scaling is independent of varied gravitational constant g and intruder mass density ρ_i/ρ_g; the plateau value at low v_0 is approximately equal to Mg, as expected. (d) F_{max}/KD is plotted as a function of ρ_i/ρ_g for the largest value of v_0 shown in (c), $v_0 \approx v_b$, showing that intruder weight has little effect on the peak force, especially when $\rho_i > 4\rho_g$. The legend in (d) applies to (c) as well.

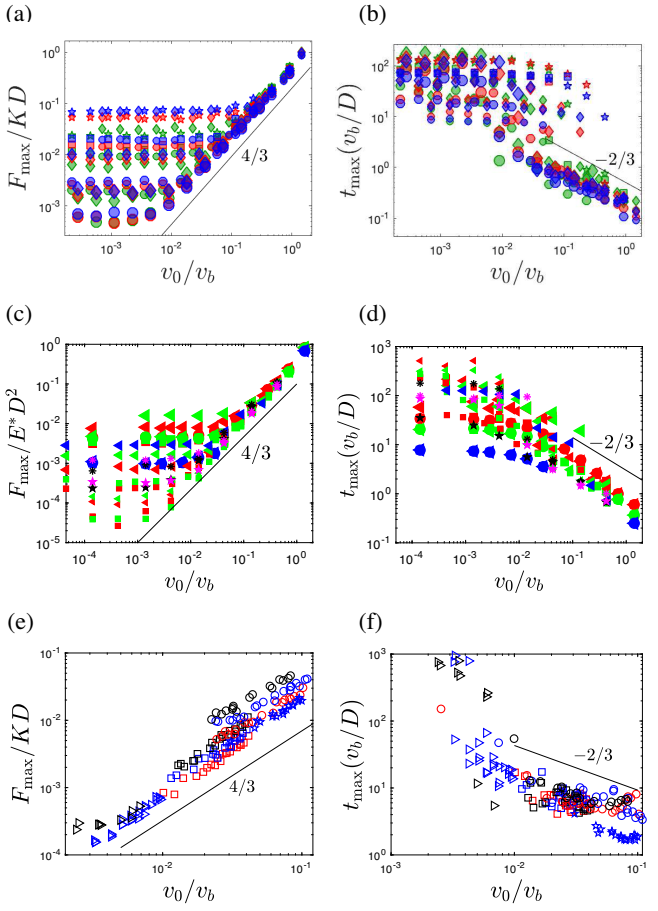

FIG. 4. Scaled plots of $F_{\max}$ and $t_{\max}$ versus v_0 for (a),(b) simulations of 2D frictionless grains with $\alpha = 1$; (c),(d) simulations of 3D frictional grains with $\alpha = 1.5$; and (e),(f) 2D frictional grains from experiment, with $\alpha \approx 1.4$. The symbols in (e),(f) are the same as Figs. 2(c) and 2(d); For simulations shown in (a)–(d), the full symbol list is given in the Supplemental Material [22]. Plateau values for small v_0/v_b are set by $F_{\max} \approx Mg$.

where $v_b = \sqrt{E^*/\rho_g}$. Figures 4(c) and 4(d) show collapsed data in 3D frictional Hertzian simulations, which are nearly identical to the 2D frictionless Hookean results shown in Figs. 4(a) and (b). Experimental results, plotted in Figs. 4(e) and 4(f), are more scattered than the simulations; this is partly expected since force is not directly measured but inferred by tracking the intruder and, in the case of hard particles, using a correction from a calibrated photoelastic signal. Experimental impacts of large intruders into soft particles appear to deviate from the scaling, which could be due to the extreme particle deformation and collective stiffening during these impacts [21].

Thus, we find universal scaling laws for the peak forces and associated timescales during the early stage of high-speed impact: $F_{\max} \propto KD(v_0/v_b)^{4/3}$ in 2D, $F_{\max} \propto E^*D^2(v_0/v_b)^{4/3}$ in 3D, and $t_{\max} \propto (D/v_b)(v_0/v_b)^{-2/3}$ in both 2D and 3D. As we now show, these scaling laws are inconsistent with Poncelet, shock, and added-mass models, suggesting that a new theory must be formulated. The scaling $F_{\max} \propto v_0^{4/3}$ is plainly inconsistent with Poncelet drag, where $F \propto v^2$. Granular shock theory [28–33], which captures the speed of propagating forces in these experiments [21], is fundamentally based on the force exponent α and states that large stresses (compared to the prestress) propagate at a shock speed v_f, where $(v_f/v_b) \propto (v_0/v_b)^{(\alpha-1)/(\alpha+1)} \propto (P_{\max})^{(\alpha-1)/(2\alpha)}$. By rearranging, $P_{\max} \propto v_0^{(2\alpha)/(\alpha+1)}$, which yields $P_{\max} \propto v_0^{6/5}$ for Hertzian grains (where $\alpha = 1.5$) and $P_{\max} \propto v_0^{7/6}$ for the disks we use (with $\alpha \approx 1.4$), which are also inconsistent with $F_{\max} \propto v_0^{4/3}$. Even a modified shock theory that somehow predicted $F_{\max} \propto v_0^{4/3}$ must be fundamentally based on α. Thus, the lack of dependence on α shown in Figs. 3(a) and 3(b) confirms that granular shock theory cannot explain our results.

A third possible explanation is added-mass effects [6, 34–36]. Added-mass models assume that the intruder, with mass M, decelerates primarily due to rigid connection to a growing mass of the material, with mass $m_a(t)$. Assuming external forces are known, a mathematical form for $m_a(t)$ will then fully determine the trajectory, including $F_{\max}$. This scenario is consistent with the images shown in Fig. 1, since there is a growing cluster of grains that is connected to the intruder. For comparison, we numerically solve added-mass dynamics (see Supplemental Material [22] for details), assuming the added mass is a half circle (in 2D) or sphere (in 3D) with a radius R that grows at the force propagation speed v_f, i.e., $R = v_f t$, as suggested by Fig. 1. This gives $m_a(t) = \pi(v_f t)^2/2$ in 2D and $m_a(t) = 2\pi(v_f t)^3/3$ in 3D, with v_f as a constant (true for a Hookean force law). Solving this model yields $F_{\max} = Av_0$ in 2D and 3D, not $F_{\max} \propto v_0^{4/3}$; $A \propto M^{1/2}$ in 2D and $A \propto M^{2/3}$ in 3D; and $t_{\max}$ independent of v_0, not $t_{\max} \propto (v_0)^{-2/3}$. It is possible that $F_{\max} \propto v_0^{4/3}$ could be obtained for some choice $m_a(t)$, but A always increases with M for the forms of $m_a(t)$ that we try, as well as in the theoretical analysis in Ref. [36] of the added-mass model from Ref. [35]. This is inconsistent with the lack of dependence on ρ_i, shown in Figs. 3(c) and 3(d).

We note that the soft repulsive disks and spheres used in the simulations are commonly used to model other soft particulate media (like foams or emulsions), suggesting that this description will likely apply to a much broader group of materials. We also note that the maximum grain compression $\delta_{\max}$ can be easily estimated from the scaling laws we show, which could be used to predict grain fracture or crushing. In 3D, with $P_{\max} = F_{\max}/D^2$, the maximum force felt by a grain is $f_{\max} \sim P_{\max}d^2 \sim d^2E^*(v_0/v_b)^{4/3}$. For the Hookean force law, $f_{\max} = E^*d\delta_{\max}$, so $\delta_{\max}/d \sim (v_0/v_b)^{4/3}$. This is why we do not show any impacts with $v_0 > v_b$: grain-grain overlaps in simulations became similar to the size of a grain. Physical grains would

certainly be crushed or fractured in this regime, and other physics would likely become dominant.

We acknowledge funding from the Office of Naval Research under Grant No. N0001419WX01519. These experiments were performed in the late R. P. Behringer's lab during dissertation work by A. H. C.. We also thank Jeffrey Haferman and Bruce Chiarelli for help with high-performance computing at NPS.

[1] D. van der Meer, Impact on granular beds, Annu. Rev. Fluid Mech. **49**, 463 (2017).
[2] W. A. Allen, E. B. Mayfield, and H. L. Morrison, Dynamics of a projectile penetrating sand, J. Appl. Phys. **28**, 370 (1957).
[3] M. J. Forrestal and V. K. Luk, Penetration into soil targets, Int. J. Impact Eng. **12**, 427 (1992).
[4] C. Glößner, S. Moser, R. Külls, S. Heß, S. Nau, M. Salk, D. Penumadu, and N. Petrinic, Instrumented projectile penetration testing of granular materials, Exp. Mech. **57**, 261 (2017).
[5] M. Omidvar, S. Bless, and M. Iskander, Recent insights into penetration of sand and similar granular materials, in *Shock Phenomena in Granular and Porous Materials* (Springer, New York, 2019), pp. 137–163, https://link.springer.com/chapter/10.1007%2F978-3-030-23002-9_5.
[6] J. Aguilar and D. I. Goldman, Robophysical study of jumping dynamics on granular media, Nat. Phys. **12**, 278 (2016).
[7] J. Aguilar, T. Zhang, F. Qian, M. Kingsbury, B. McInroe, N. Mazouchova, C. Li, R. Maladen, C. Gong, M. Travers, R. L. Hatton, H. Choset, P. B. Umbanhowar, and D. I. Goldman, A review on locomotion robophysics: The study of movement at the intersection of robotics, soft matter and dynamical systems, Rep. Prog. Phys. **79**, 110001 (2016).
[8] S. J. Robbins and B. M. Hynek, A new global database of mars impact craters ≥ 1 Km: 1. Database creation, properties, and parameters, J. Geophys. Res. **117**, E05004 (2012).
[9] H. J. Melosh, *Impact Cratering: A Geologic Process* (Oxford University Press, New York, 1989).
[10] H. Katsuragi and D. J. Durian, Unified force law for granular impact cratering, Nat. Phys. **3**, 420 (2007).
[11] D. I. Goldman and P. Umbanhowar, Scaling and dynamics of sphere and disk impact into granular media, Phys. Rev. E **77**, 021308 (2008).
[12] P. Umbanhowar and D. I. Goldman, Granular impact and the critical packing state, Phys. Rev. E **82**, 010301(R) (2010).
[13] S. J. Bless, M. Omidvar, and M. Iskander, Poncelet coefficients for dry sand, AIP Conf. Proc. **1979**, 110001 (2018).
[14] M. P. Ciamarra, A. H. Lara, A. T. Lee, D. I. Goldman, I. Vishik, and H. L. Swinney, Dynamics of Drag and Force Distributions for Projectile Impact in a Granular Medium, Phys. Rev. Lett. **92**, 194301 (2004).
[15] S. Bless, W. Cooper, K. Watanabe, and R. Peden, Deceleration of projectiles in sand, AIP Conf. Proc., **1426**, 45 (2012).
[16] A. H. Clark and R. P. Behringer, Granular impact model as an energy-depth relation, Europhys. Lett. **101**, 64001 (2013).
[17] A. H. Clark, A. J. Petersen, and R. P. Behringer, Collisional model for granular impact dynamics, Phys. Rev. E **89**, 012201 (2014).
[18] M. Tiwari, T. R. K. Mohan, and S. Sen, Drag-force regimes in granular impact, Phys. Rev. E **90**, 062202 (2014).
[19] C. S. Bester and R. P. Behringer, Collisional model of energy dissipation in three-dimensional granular impact, Phys. Rev. E **95**, 032906 (2017).
[20] A. H. Clark, L. Kondic, and R. P. Behringer, Particle Scale Dynamics in Granular Impact, Phys. Rev. Lett. **109**, 238302 (2012).
[21] A. H. Clark, A. J. Petersen, L. Kondic, and R. P. Behringer, Nonlinear Force Propagation during Granular Impact, Phys. Rev. Lett. **114**, 144502 (2015).
[22] See Supplemental Material at http://link.aps.org/supplemental/10.1103/PhysRevLett.124.178002 for additional supporting figures, details of simulations, and additional detail regarding comparison with added-mass models.
[23] P. A. Cundall and O. D. L. Strack, A discrete numerical model for granular assemblies, Géotechnique **29**, 47 (1979).
[24] A. H. Clark, L. Kondic, and R. P. Behringer, Steady flow dynamics during granular impact, Phys. Rev. E **93**, 050901 (R) (2016).
[25] S. Plimpton, Fast parallel algorithms for short-range molecular dynamics, J. Comput. Phys. **117**, 1 (1995).
[26] J. J. S. Jerome, N. Vandenberghe, and Y. Forterre, Unifying Impacts in Granular Matter from Quicksand to Cornstarch, Phys. Rev. Lett. **117**, 098003 (2016).
[27] P.-E. Peyneau and J.-N. Roux, Frictionless bead packs have macroscopic friction, but no dilatancy, Phys. Rev. E **78**, 011307 (2008).
[28] V. F. Nesterenko, A. N. Lazaridi, and E. B. Sibiryakov, The decay of soliton at the contact of two "acoustic vacuums", J. Appl. Mech. Tech. Phys. **36**, 166 (1995).
[29] C. Daraio, V. F. Nesterenko, E. B. Herbold, and S. Jin, Strongly nonlinear waves in a chain of teflon beads, Phys. Rev. E **72**, 016603 (2005).
[30] S. Job, F. Melo, A. Sokolow, and S. Sen, How Hertzian Solitary Waves Interact with Boundaries in a 1D Granular Medium, Phys. Rev. Lett. **94**, 178002 (2005).
[31] C. Daraio and V. F. Nesterenko, Strongly nonlinear wave dynamics in a chain of polymer coated beads, Phys. Rev. E **73**, 026612 (2006).
[32] L. R. Gómez, A. M. Turner, M. van Hecke, and V. Vitelli, Shocks near Jamming, Phys. Rev. Lett. **108**, 058001 (2012).
[33] S. van den Wildenberg, R. van Loo, and M. van Hecke, Shock Waves in Weakly Compressed Granular Media, Phys. Rev. Lett. **111**, 218003 (2013).
[34] T. T. Truscott, B. P. Epps, and J. Belden, Water entry of projectiles, Annu. Rev. Fluid Mech. **46**, 355 (2014).
[35] S. R. Waitukaitis and H. M. Jaeger, Impact-activated solidification of dense suspensions via dynamic jamming fronts, Nature (London) **487**, 205 (2012).
[36] S. Mukhopadhyay, B. Allen, and E. Brown, Testing constitutive relations by running and walking on cornstarch and water suspensions, Phys. Rev. E **97**, 052604 (2018).